Deep Resources Engineering 1 (2024) 100109

Contents lists available at ScienceDirect

Deep Resources Engineering

journal homepage: www.keaipublishing.com/en/journals/deepre/

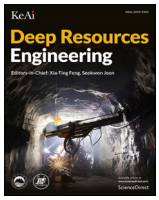

Full Length Article

Crustal structure and shallow-focus seismic activities in the Sumatra subduction zone: Constrains from receiver function inversion

Xuelei Li [a,*], Yuan Wang [b], Tianyao Hao [b], Yuxin Yuan [a], Zhuo Jia [c], Jinpeng Luan [d]

[a] School of Microelectronics and Physics, Hunan University of Technology and Business, Changsha 410205, China
[b] Key Laboratory of Petroleum Resource Research, Institute of Geology and Geophysics, Chinese Academy of Sciences, Beijing 100029, China
[c] School of Civil Engineering, Changsha University of Science & Technology, Changsha, Hunan 410114, China
[d] College of Resources and Civil Engineering, Northeastern University, Shenyang 110819, China

ARTICLE INFO

Keywords:
Sumatra
Receiver function
Subduction plate
Seismic activities

ABSTRACT

The Sumatra subduction zone is located in the southwest of the Suna plate, between the Euro-Asia Plate and Indo-Austrilian Plates. With the obliquely subducting of the Indo-Austrilian Plate toward the the Euro-Asia Plate, complex tectonics, strong earthquakes and volcanoes have been observed in this area which has become a well experimental field used to study the subduction zone. In this work, we employed receiver function method to evaluate the S-wave velocity structure beneath 5 broadband seismic stations along the Sumatra subduction zone. We selected 332 receiver function waveforms with intelligent software and manual picking methods, including 130, 34, 42, 29 and 97 receiver function waveforms corresponding to BKNI, GSI, LHMI, MNAI, and PMBI stations, respectively. These stacked receiver function waveforms were applied to inversion to estimate Swave structure beneath each station based on a Neighborhood Algorithm (NA). Our results indicate that the sediment layers for GSI, LHMI and MNAI stations are more than 3 km thick, two stations of which are thicker than 6 km (e.g. GSI and LHMI). The difference of receiver function waveforms for NE, SW and W orientation at station GSI where is accompanied with strong thrust earthquakes suggests that there is a complicated structure beneath this station. Station BKNI and PMBI are located on the eastern side of the Sumatra fault and the thickness of their sediment layers is only ~ 1 km. The crustal thickness for back-arc basin is within 30–36 km. However, the crustal thickness of forearc area varies from ~ 26 km of the forearc ridge to 26–30 km of the forearc basin toward continent and its, which suggests that the down dip limit (slab-Moho intersection) of seismogenic zone is within 29–36 km in forearc and explains why the shallow-focus earthquakes play a dominant role in this area. The stable state for the inner wedge of forearc within a seismogenic circle provides a favorable environment for storing stress. Meanwhile, these faults caused by the subducting of Indo-Austrilian Plate constructed a condition (e.g. cracking of intact rocks and frictional sliding) in which it would trigger shallow-focus seismic activities (releasing stress).

1. Introduction

The Sumatra subduction zone is located between the Eurasian plate and the Indo Australian plate, on the southwestern margin of the Sunda landmass (Fig. 1). Due to the subduction of the Indo Australian plate to the Eurasian plate, the region has experienced an extremely complex tectonic evolution process [1–8]. A large number of seismic tomography studies have revealed three-dimensional images of the lithospheric structure of the Sumatra subduction zone [9–15], providing a good prior model for the study of the small-scale deep dynamic characteristics in the front of the Mentawai arc.

Sumatra subduction zone is an area with strong seismicity. From 1900 to 0:00 on January 1, 2018, there were 10,041 earthquakes with Ms = 3.0–10, including 32 earthquakes with Mw ≥ 7.0, which can be shown in Fig. 1. In the 300 years before 2004, three large earthquakes (1797, 1833, 1861) were recorded in history, which formed the main fault in front of arc at present (Fig. 1); since 2004, five large earthquakes (2004, 2005, 2007a, 2007b, 2010) have occurred in the study area.

According to McCaffrey's study of seismic slip vector, it is shown that the pre arc lobes between the Sumatra fault and the subduction trench are extending northwestward [16,17]. His model implies that the front arc is not rigid, but extends at a uniform strain rate of 1–3 × 10^{-8}

* Corresponding author.
E-mail address: lixuelei@hutb.edu.cn (X. Li).

https://doi.org/10.1016/j.deepre.2024.100109
Received 29 May 2024; Received in revised form 27 July 2024; Accepted 31 July 2024
Available online 8 August 2024

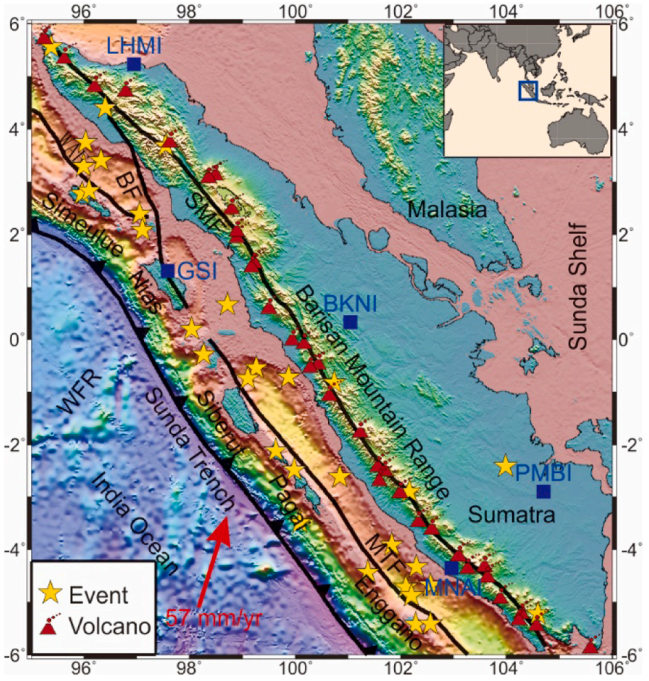

Fig. 1. Map showing the seismic stations, large earthquakes (Mw ≥ 7.0) and volcanoes along the Sumatra subduction zone. Blue rectangles mark the seismic stations. Black lines denote the fault zones, such as SMF- Sumatra Fault, MTF-Mentawai Fault, BF-Batee Fault and WAF-West Andaman Fault. The bold line with triangles indicates the boundary of plate. Volcanoes are presented as dark red triangles with dots. Yellow Stars show all large earthquakes in this area (Data from USGS, 1900–2018 Mw ≥ 7.0). Wharton Fossil Ridge (WFR) and convergence vector [14] are also shown.

mm/yr, but the deformation caused by stretching is not clearly understood. McCaffrey infers that the front of the arc will be stretched by normal faults that form the forearc basin and also by strike slip faults. Therefore, the fault will cross the subduction trench to the fore arc area of Sumatra fault. However, there is no conclusive evidence for extension deformation or pre arc stretching [18,19].

Diament et al. point out that there is more than one strike slip fault parallel to the arc in front of the arc [20], indicating that the horizontal arc shear is acceptable and the discovery of the Mentawai fault provides evidence for this model in 1992 (Fig. 2). The 600 km long Mentawai fault is located in the eastern part of the Mentawai islands, which are the boundary between the fore arc ridge and the fore arc basin. Diament et al. believe that this situation is similar to that of Sumatra fault, and the linear normal flower structure of Mentawai fault is typical of large-scale strike slip fault, which explains a small amount of movement parallel to trench. At the same time, they observed these movements along the Sumatra subduction zone in South Sumatra (Fig. 2).

The study of high-resolution reflection seismology and bathymetric data did not find any evidence of strike slip movement [21]. Instead, they found that the mindawai fault is a series of Southwest dipping thrust faults. This result supports the original explanation of karig which the mindawai fault is a recoil fault with strike slip movement [22].

Kumar et al. pointed out in 2013 that the seismogenic zone near the front arc of Sumatra subduction zone is extremely developed due to the fact that the deep fault becomes the channel for upward transmission of dehydrated fluid from subducted plate [23]. Regional tomography and seismic relocation results reveal that there are two seismogenic regions in front of the mingdawei arc, with a depth of 25–30 km [24]. In recent years, the rupture depths of the four major earthquakes in front of the mindawai arc are between 20 and 35 km (MW 8.4 2007, MW 7.9 2007, MW 7.2 2008, MW 7.7 2010). According to the research results of receiver function, the crustal thickness in the forearc area increases from

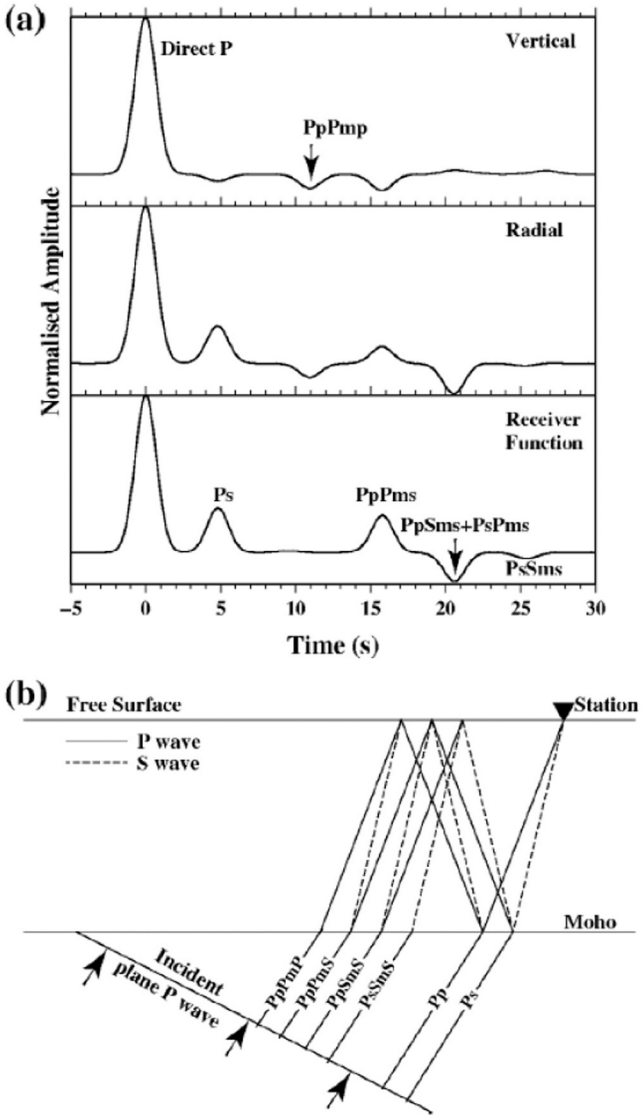

Fig. 2. Sketch of receiver function principle [32]. (a) Radial receiver function obtained from deconvolution of vertical from the radial component; (b) Ray sketch of different phase.

~ 26 km of the forearc ridge to 26–30 km near the continental side of the forearc basin, which further indicates that the seismogenic area is mainly developed near the crust mantle boundary zone. However, previous studies mainly focus on exploring the subduction plate and the rupture mechanism of large earthquakes, and there is no systematic study on the dynamic mechanism among the crustal structure, seismogenic zone and subduction plate. The focal depth information of velocity structure is the key to explore the dynamic characteristics of Sumatra subduction zone, it can also provide reference for seismic activity analysis and earthquake prevention and mitigation.

In this study, the velocity discontinuity and S-wave velocity structure under the stations are studied by using the receiver function method based on the recorded data of five broadband fixed seismic stations.

Based on the research results of receiver function method, combined with seismic activity characteristics, fault distribution and other regional geological data, the crustal structure and geodynamic characteristics of Sumatra subduction zone are revealed, which provides new Seismological Evidence for the structural evolution of Sumatra subduction zone.

Table 1
Information for five broadband seismic stations along Sumatra.

Station code	Longitude	Latitude	Elevation (m)
BKNI	101.04	0.33	51
GSI	97.58	1.30	107
LHMI	96.94	5.22	3
MNAI	102.96	− 4.36	154
PMBI	104.77	− 2.92	30

2. Data and methods

2.1. Receiver function

In 1979, Langston proposed a method to separate radial and tangential receiver functions from teleseismic P-wave waveform data based on the equivalent source assumption [25]. Owens et al. applied this method to broadband seismic records in 1984 and proposed a linear inversion method of receiver function under the assumption of homogeneous layered medium in the crust [26]. Since the receiver function method has a high vertical resolution (generally 1 km), it can not only obtain the S-wave velocity structure under the station, but also has a good constraint on the converted wave interface [27–29]. This method has been widely used since it was proposed and its theory and method have been constantly improved and developed [30,31].

In short, the receiver function is related to the teleseismic rays sampled from the earth's medium along the propagation path. By eliminating the influence from the source and propagation path, the local impulse response of the media under the seismic station can be obtained which can be used to retrieve the velocity structure and discontinuity information under the seismic station. The receiver function waveform carries a lot of local multiple information, as shown in Fig. 2, such as PpPmP、PpPmS、PpSmS、PsSmS, etc [32].

If we make an ideal assumption of various effects, three kinds of propagation responses are applied to the source time function to form a series linear system. In addition, the instrument response $I(t)$ should be considered and the final system output will produce displacement $u(t)$. This series representation corresponds to a convolution model. Because of the superposition effect of linear system, convolution can be performed. In the time domain, the system is expressed as follows:

$$\begin{aligned} u_V(t) &= s(t)*N_S*P(t)*N_{R_V}*I(t) \\ u_R(t) &= s(t)*N_S*P(t)*N_{R_R}*I(t) \\ u_T(t) &= s(t)*N_S*P(t)*N_{R_T}*I(t) \end{aligned} \tag{1}$$

where $u_V(t)$, $u_R(t)$, $u_T(t)$ and represent the vertical component, radial component and tangential component of the seismic record respectively, and the asterisk represents convolution operation. The above formula is converted to frequency domain as follows:

$$\begin{aligned} u_V(w) &= s(w) \times N_S \times P(w) \times N_{R_V} \times I(w) \\ u_R(w) &= s(w) \times N_S \times P(w) \times N_{R_R} \times I(w) \\ u_T(w) &= s(w) \times N_S \times P(w) \times N_{R_T} \times I(w) \end{aligned} \tag{2}$$

The common terms of the three components in Formula (1) and (2) can be eliminated by deconvolution, where and are the required radial and tangential receiving functions. At present, there are two kinds of commonly used methods to separate receiver functions, one is time domain deconvolution, the other is frequency domain deconvolution. The receiver function extracted by time domain deconvolution method

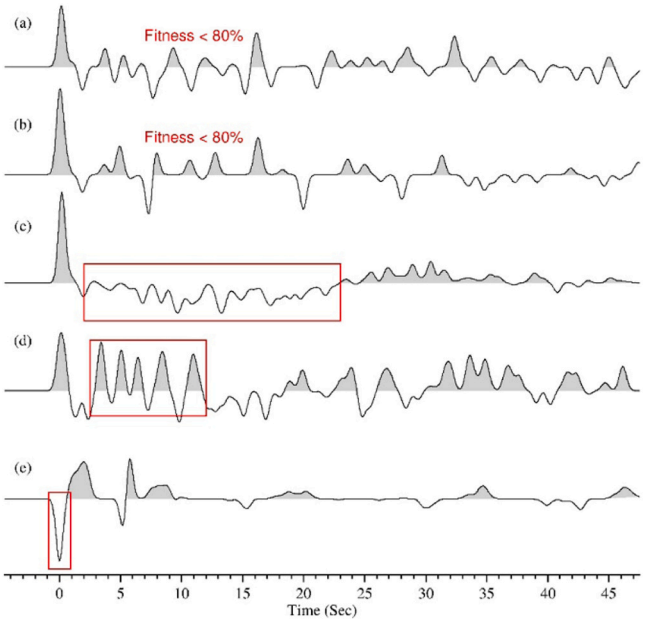

Fig. 4. The principle of receive function picking. (a) and (b) fitness of the radial component and convolution between receiver function and vertical component no more than 80 %. (c) lacking of Ps and multiple wave phases. (d) amplitude of translating phase is too big. (e) first P-wave phase is minus.

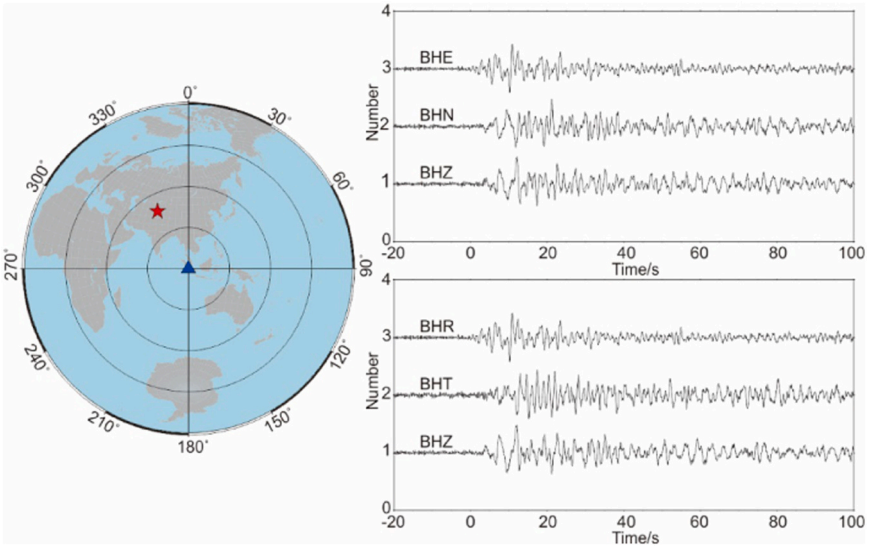

Fig. 3. Sketch of three component seismic data translated from ENZ to RTZ direction.

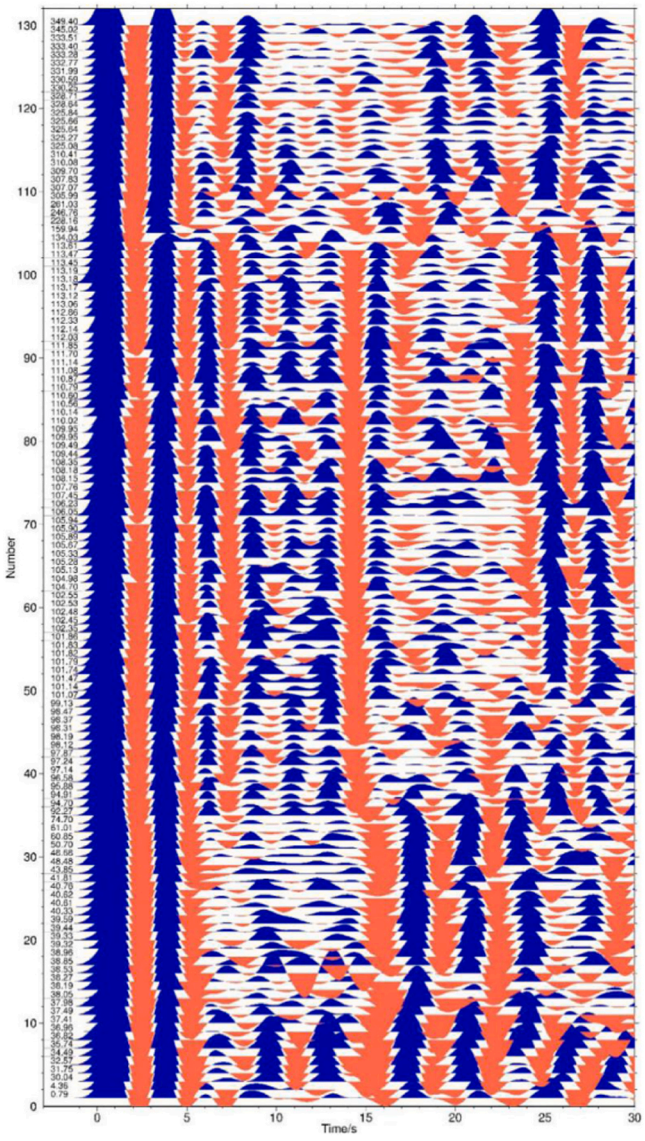

Fig. 5. Receiver function ranking for BKNI. Left fonts denote the back azimuth.

has less background noise and has no limit on the recording length of seismic waveform, which is beneficial to the study of time domain using receiver function (such as receiver function migration imaging); frequency domain deconvolution method can achieve trade-off between signal-to-noise ratio and resolution of receiver function, which is beneficial to waveform research such as receiver function inversion. In this paper, the time domain deconvolution method is used to extract the receiver function.

2.2. Iterative deconvolution in time domain

Time domain iterative deconvolution is different from frequency domain deconvolution. It decomposes time series into time-shift superposition of pulse wavelet $h(t)$with different assignment values, and then iterates step by step. The mathematical formula is as follows:

$$< rf(t) >= \sum_i m_i h(t - t_i) \tag{3}$$

When the error of the following formula is a minimum, $\nabla^2\varphi = \frac{1}{c^2(x_i)}\ddot{\varphi}$ and $\varphi(x_i)$ can be obtained,

$$\Delta_1 = \int_{-\infty}^{+\infty} \left| R(t) - m_1 h\left(t - t_1\right) \otimes Z(t) \right|^2 dt \tag{4}$$

If Δ_1 is to be derivative of m_1, the corresponding $m_1$can be expressed as follows:

$$m_1 = \frac{\int_{-\infty}^{+\infty} R(t)Z(t - t_1)dt}{\int_{-\infty}^{+\infty} Z^2(t)dt} \tag{5}$$

$$\Delta_1 = \frac{\int_{-\infty}^{+\infty} R(t)^2 dt - \left[\int_{-\infty}^{+\infty} R(t)Z(t - t_1)dt\right]^2}{\int_{-\infty}^{+\infty} Z^2(t)dt} \tag{6}$$

Therefore, if Δ_1 is a minimum and $\left[\int_{-\infty}^{+\infty} R(t)Z(t - t_1)dt\right]^2$ is a maximum, then t_1 can be obtained and the value of m_1 can be obtained. Finally, $m_1 h(t - t_1)$ is subtracted from $R(t)$ and $R(t)$ is replaced by $R'(t)$. based on the same operation flow, m_2 and t_2 are obtained :

$$R'(t) = R(t) - m_1 h(t - t_1) \tag{7}$$

The next iteration of the loop can obtain m_i and t_i. if Δ_{N+1} does not decrease significantly, the iteration stops. The corresponding receiver function can be obtained by introducing (m_i, t_i) into formula 3 and Gaussian filtering, and the final solution error is Δ_{N+1}.

2.3. Receiver function inversion

According to the measured seismic observation data, the receiver function waveform is extracted, and the theoretical receiver function is calculated after the initial input model is given. In order to solve the error between the theoretical receiver function and the observed receiver function waveform, it is necessary to iterate and update the model. If the error between the observed receiver function and the theoretical receiver function is minimal, the final S-wave velocity structure model can be obtained. This process is called receiver function waveform inversion method. Receiver function inversion is essentially a non-linear problem. Linear inversion is linearized based on the first-order partial differential operator of nonlinear function. In general, it can fit the waveform of observation receiver function well by using multiple underground medium model parameters. However, it is difficult to guarantee the reliability of the inversion results because of the non uniqueness of the receiver function of the relatively complex geological model. More importantly, the linear inversion method strongly depends on the initial velocity model and the inversion results are affected by too many velocity layers [33]. In contrast, the nonlinear inversion method, especially the global optimization algorithm, can invert the main parameters of the underground medium with a small number of initial model parameters. At the same time, if VP/VS and anisotropy exist, the relatively accurate velocity structure can also be found. Therefore, the receiver function nonlinear inversion method has been widely studied and applied since it was proposed. Sambridge proposed a neighborhood search algorithm in 1999, which derived the parameter search space based on Tyson unit [34]. A derivative free adaptive search strategy is adopted to search for the optimal model with only two adjustment parameters. In this study, the crustal velocity structure is inversed by this method.

2.4. Data sources

The data of five broadband seismic stations in Sumatra subduction zone are used in this study, as shown in Fig. 1. Four stations (LHMI, BKNI, MNAI, PMBI) on Sumatra island and one station (GSI) on Nias island are included. The five stations belong to the Ge network under the GEOFON data center and are deployed by the Potsdam geoscience Center (GFZ).

GSI stations are located on the fore arc ridge of Sumatra subduction zone, LHMI, BKNI and PMBI are located in the back arc basin of Sumatra

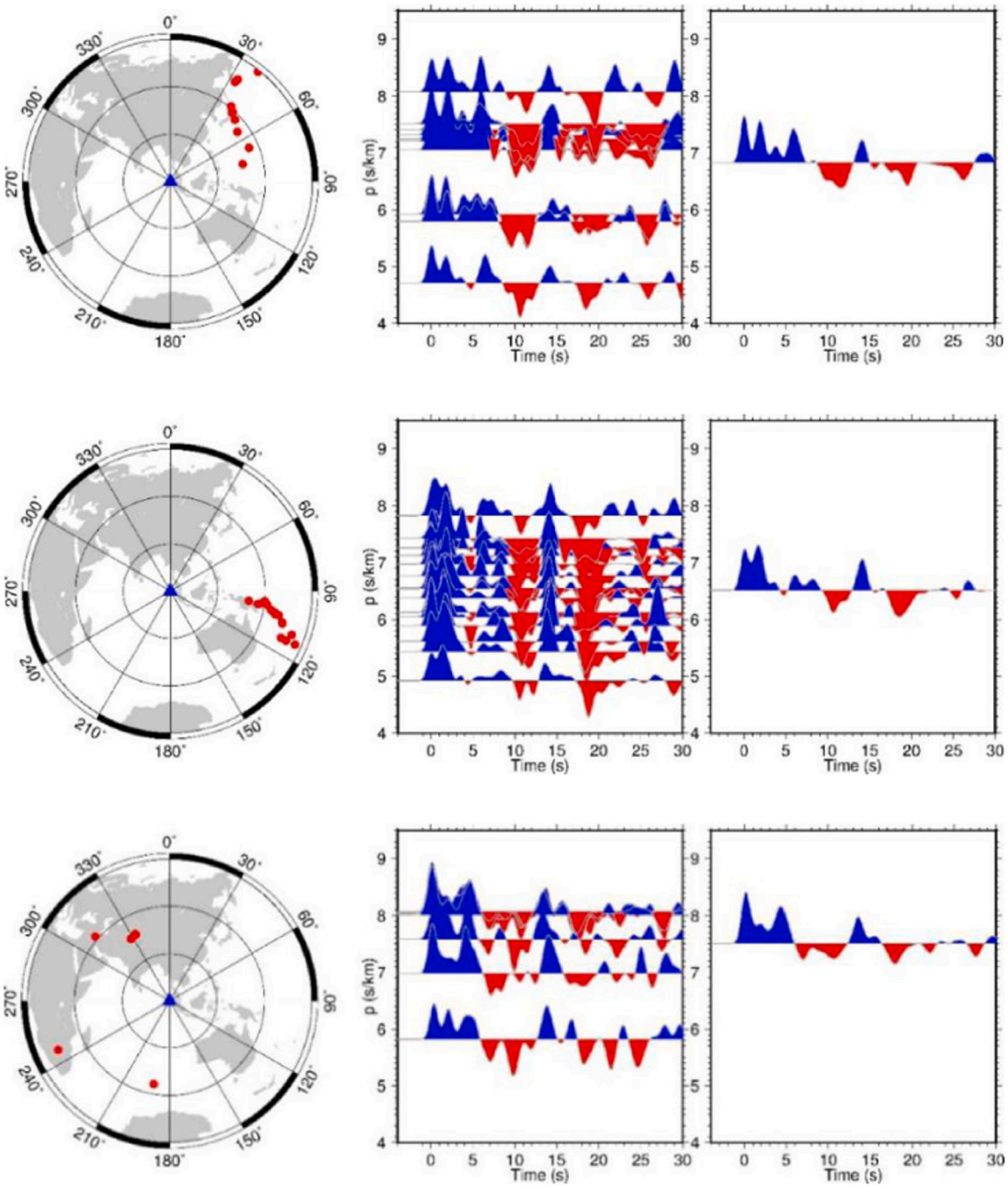

Fig. 6. Results of receiver function waveforms stacking by ray parameter for NE, SE and W direction at the GSI station. Left panels present teleseismic events of each direction. Middle panels show receiver function waveforms ranking by ray parameter. Right panels indicate the average receiver function after stacking.

Table 2
Initial reference model.

Horizon	Thickness (km)	Top S-wave velocity(km/s)	Bottom S-wave velocity(km/s)	V_P/V_s
Sedimentary layer	2	2.6	2.8	2.80
Crystalline substrate	1	2.8	2.9	1.80
Upper crust	13	3.0	3.6	1.75
Middle crust	15	3.6	3.8	1.75
Lower crust	8	3.8	4.0	1.75
Upper mantle	20	4.3	4.4	1.80

Table 3
Space parameter for an inversion model.

Horizon	Thickness (km)	Top S-wave velocity(km/s)	Bottom S-wave velocity(km/s)	V_P/V_s
Sedimentary layer	0–8	1.0–4.0	1.0–4.0	1.8–3.0
Crystalline substrate	0–3	1.0–4.4	2.0–4.4	1.5–2.0
Upper crust	5–15	1.0–4.4	2.6–4.6	1.5–2.0
Middle crust	5–15	2.8–4.6	3.0–4.6	1.5–2.0
Lower crust	5–15	3.0–4.6	3.0–4.6	1.5–2.0
Upper mantle	10–30	3.6–5.0	3.6–5.0	1.7–2.0

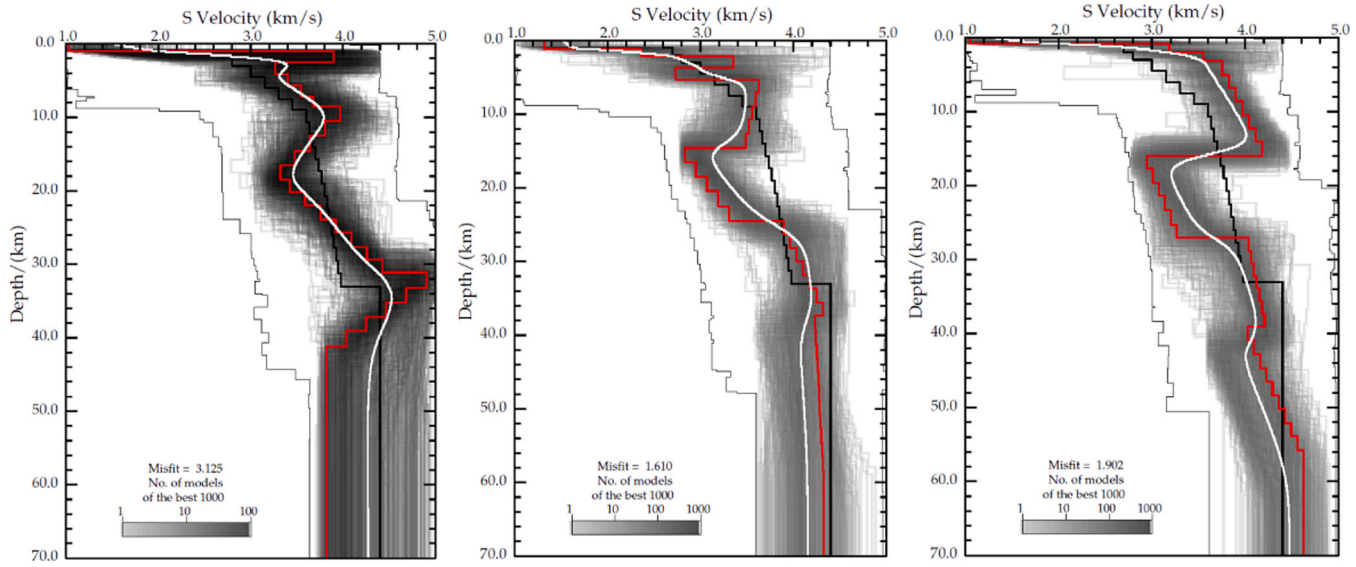

Fig. 7. S-wave velocity structure of BKNI station. Left, center and right panels present the results of receiver function inversion for NE, SE and W orientation, respectively. For each panel, gray range denotes search space; black line marks the initial reference model; red line shows the best inversion model; white curve indicates the average model of the best 1000 models, that is, as our final model.

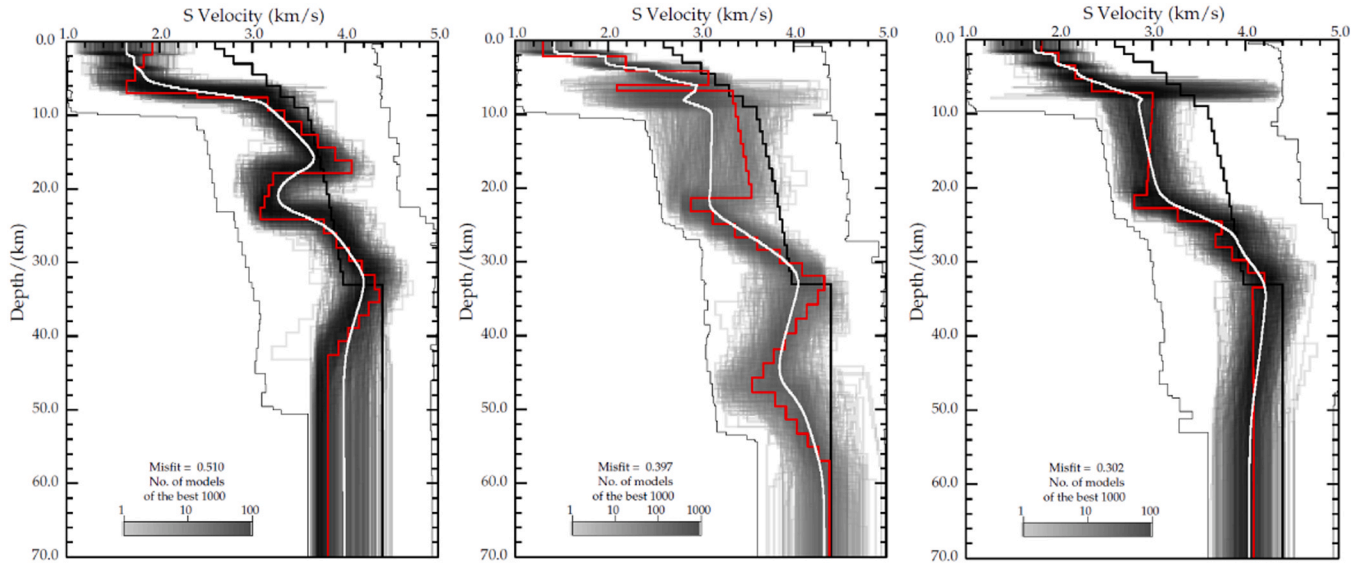

Fig. 8. S-wave velocity structure of the GSI station. Other introduction is similar to Fig. 7.

subduction zone, and MNAI is located near the continental side of the front arc basin edge of Sumatra subduction zone, as shown in Table 1. In this study, the event waveform data (Mb $\geq$ 5.5) for three years from January 2015 to December 2017 was applied from geofon data center. The epicenter distance range was 0–90° and the seismic waveform records were intercepted after preprocessing the original vertical seismic waveform. There are two methods for waveform interception. One is to calculate the theoretical arrival time of seismic wave from the source to the station according to the standard earth model, determine the waveform time window relative to the time of earthquake occurrence and then intercept the waveform of seismic events from the recorded data; The other one is to intercept the waveform of earthquake events according to the time of earthquake occurrence.

Firstly, the original waveform data are selected to obtain high-quality three-component seismic waveform data in accordance with teleseismic tomography. Teleseismic events are selected according to the following principles: (1) the epicenter distance is between 30° and 90° to avoid the influence of complex structure of lower mantle and core mantle boundary on teleseismic P-wave travel time; (2) the magnitude of earthquake is greater than 5.5 (Mb > 5.5) to ensure high signal-to-noise ratio. Since the time domain iterative deconvolution can effectively suppress the background noise data, for the Sumatra subduction zone with relatively complex crustal structure, the effective signal with high signal-to-noise ratio can be preserved by using this method to extract the receiver function. The prime minister rotates the original three-component teleseismic waveform data to the RTZ direction, as shown in Fig. 3, and then uses the time domain iterative deconvolution method to extract the receiver function. In order to avoid the interference of excessive high-frequency noise, the Gaussian factor is 1.5 (0.72 Hz), and the time window removes 20 s before the P-wave and 100 s after the P-wave.

After the receiver function is extracted, a very important step is to select the receiver function to obtain the receiver function with high signal-to-noise ratio. In order to improve the efficiency of receiver

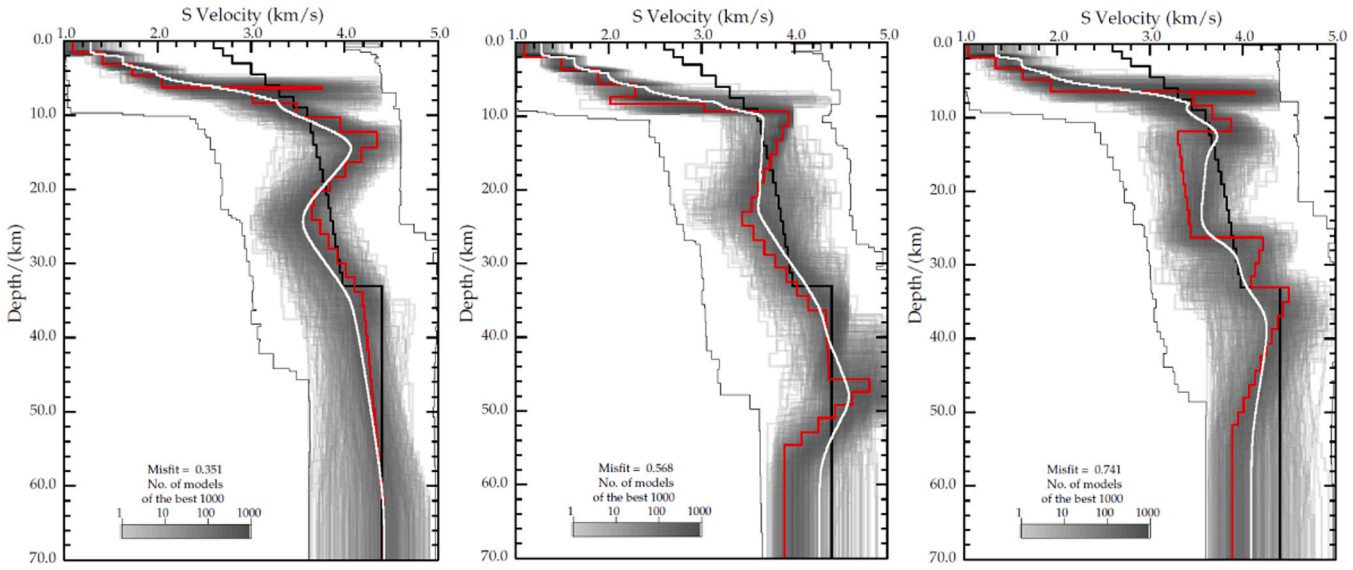

Fig. 9. S-wave velocity structure of the LHMI station. Other introduction is similar to Fig. 7.

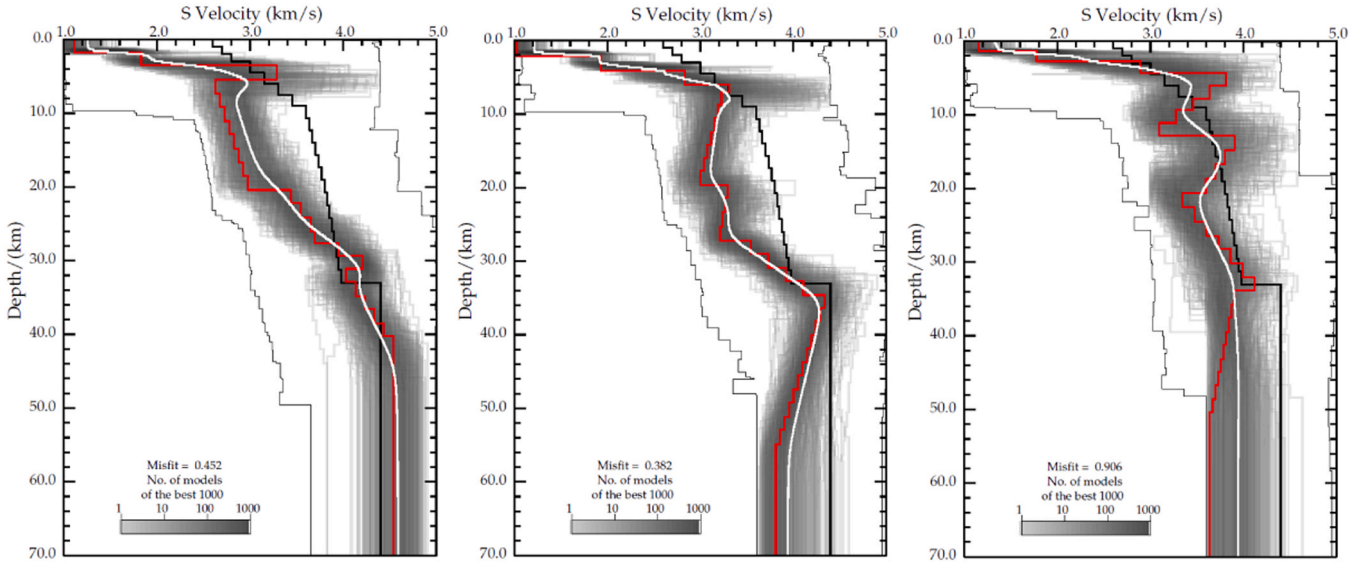

Fig. 10. S-wave velocity structure of the MNAI station. Other introduction is similar to Fig. 7.

function selection and avoid the error caused by human selection as far as possible, this study uses a set of automatic receiver function selection tools, as shown in Fig. 4. The operation process is mainly divided into four steps.

1. The extracted receiver function is convoluted with the vertical component and the convolution result is cross correlated with the radial component obtained by rotation. The receiver function whose cross-correlation fit degree is higher than 80 % is selected;
2. According to the amplitude of first arrival direct wave, the receiving function with negative amplitude of direct P wave is deleted;
3. After the first and second steps are executed, the receiver functions are superimposed to obtain the average receiver function and the cross-correlation operation is performed between each receiver function and the average receiver function. The cross-correlation window time is from 1 second to 2 s after P-wave, and the receiver functions with cross-correlation number less than 0.6 are eliminated;

According to steps 1, 2 and 3, the bad receiver function is selected and the receiver function with low signal-to-noise ratio and obvious phase error is eliminated.

After the above selection process is completed, BKNI selects 130 receiver functions. As shown in Fig. 5, GSI selects 34 receiver functions, LHMI selects 42 receiver functions, MNAI selects 29 receiver functions, and PMBI selects 97 receiver functions.

2.5. *Receiver function inversion*

In order to improve the signal-to-noise ratio of the receiver function and obtain more accurate S-wave velocity structure information, according to the waveform characteristics of the receiver function, we take the research area as the center, and divide the receiver function into NE, SE and W according to the inverse azimuth angle (Fig. 6) and stack the receiver functions of each azimuth to obtain the three azimuth average receiver functions, which are used for inversion calculation.

Due to the strong nonlinearity of receiver function inversion, the non uniqueness of receiver function inversion and the dependence of linear inversion on initial model were discussed by Ammon et al. [35].

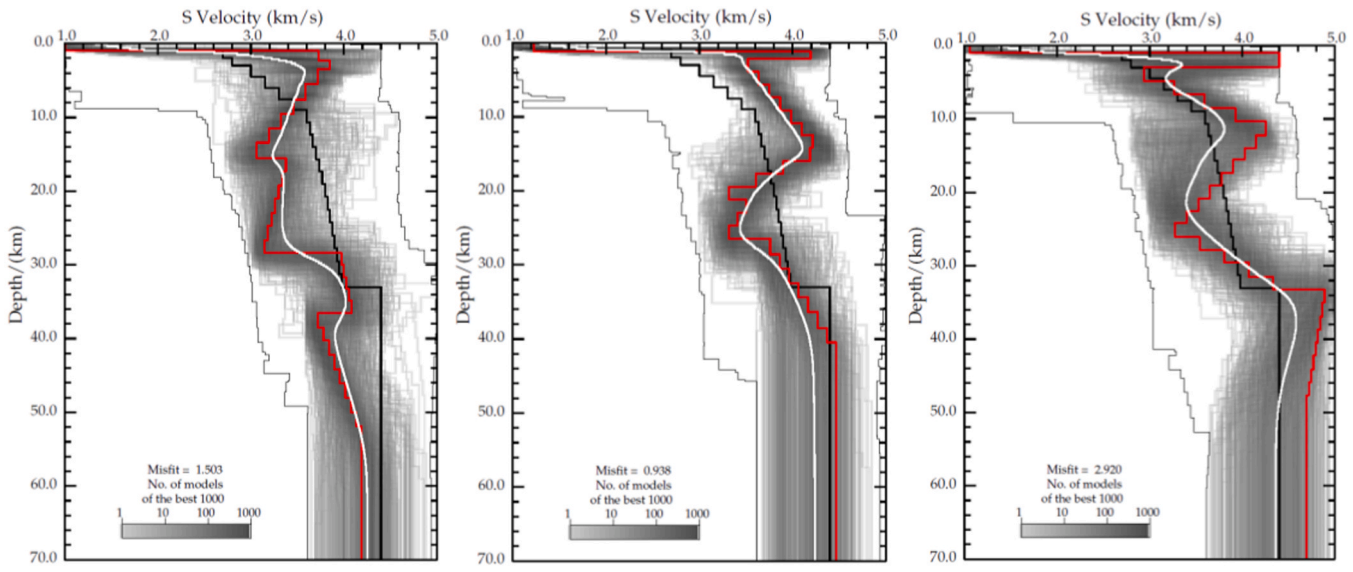

Fig. 11. S-wave velocity structure of the PMBI station. Other introduction is similar to Fig. 7.

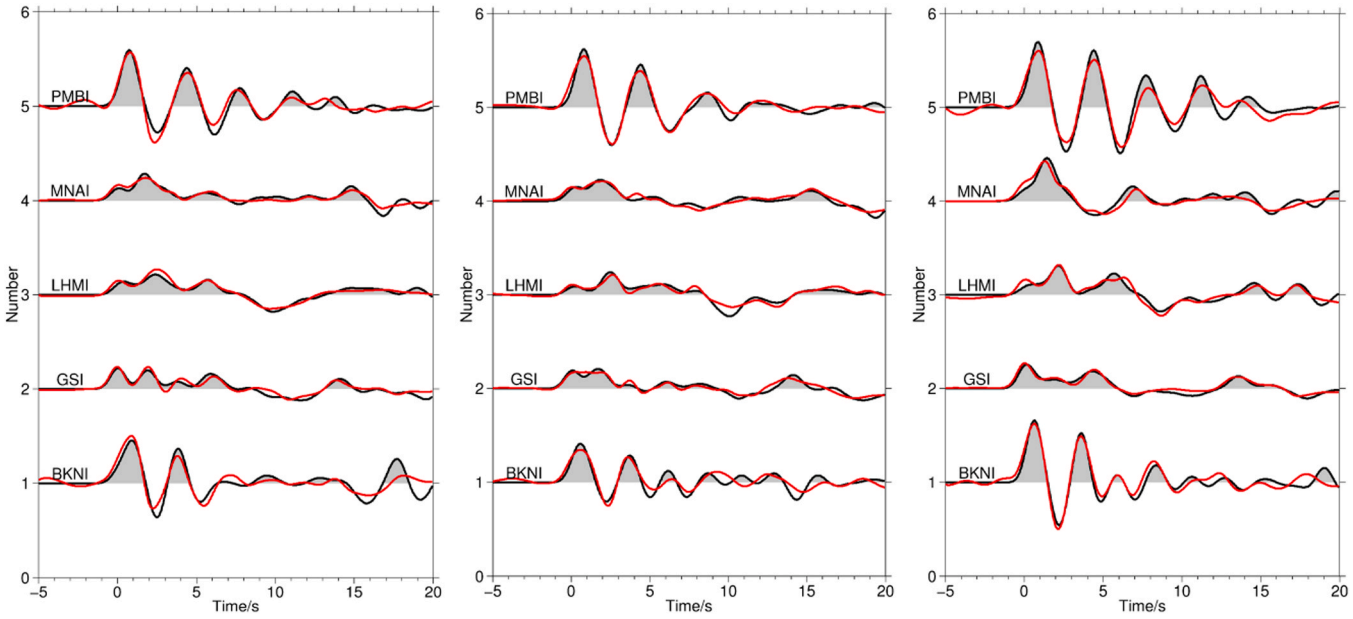

Fig. 12. Results of receiver function waveforms fitting for five stations. Left, center and right panels present the results of receiver function inversion for NE, SE and W orientation, respectively. For each panel, black waveforms filled with gray range denote the average of observation receiver function waveforms; red waveforms show the receiver function waveforms corresponding to the best inversion model.

Therefore, this paper uses the neighborhood algorithm (NA) proposed by sambridge to carry out receiver function inversion. NA algorithm is a kind of nonlinear search algorithm with strong adaptive search ability.

Given the reference model and the model search space, the theoretical receiver function corresponding to the optimal model was synthesized by Thomson Haskell matrix method according to the best model obtained in each iteration, and then calculate the mismatch value between the theoretical receiver function and the observed receiver function corresponding to the optimal model until the mismatch value converges and reaches the minimum and the optimal inversion model can be obtained.

Before inversion, the appropriate initial reference model and model search space are given. The model parameters are as follows: target layer thickness, S-wave velocity at the top and bottom of the target layer, and the corresponding wave velocity ratio. The velocity in the layer increases with the depth.

Table 2 and Table 3 show the initial reference model and its spatial parameters, which refer to the existing research results in this area [36, 37]. The inversion steps are summarized as follows:

1. Sample n_s in model space is obtained by Voronoi cells;
2. Calculate the mismatch function between the receiver function and the observed receiver function of the generation model, and select the model n_s with the minimum mismatch value;
3. Create a new model space sample n_s in the filtered n_s model space;
4. Repeat step 2 until the minimum mismatch function is obtained.

Through the trial calculation of different spatial samples, the following inversion parameters are finally determined: the sampling points in Voronoi cells model space, the minimum mismatch function

Table 4
Contrast of sediment and crust thickness from different studies.

Station code	Sediment thickness(km)	Crustal thickness (km)	Refs.
BKNI	1.0	29	Macpherson
	1.0	30	Harmon
	1.0	27–30	Bora
	1.0	31	CRUST1.0
	1.0(NE)	29(NE)	Present study
	2.0(SE)	32 (SE)	
	1.0(W)	30(W)	
GSI	4.0	30	Macpherson
	5.0	32	Kieling [40]
	3.0	19	Bora
	2.0	27	CRUST1.0
	7.0(NE)	26 (NE)	Present study
	6.0(SE)	26 (SE)	
	7.0(W)	26 (W)	
LHMI	5.0	30	Macpherson
	7.0	35	Bora
	5.0	30	CRUST1.0
	6.0(NE)	29 (NE)	Present study
	7.0(SE)	36 (SE)	
	6.0(W)	27(W)	
MNAI	2.0	16	Macpherson
	4.0	31	Bora
	4.0	26	CRUST1.0
	4.0(NE)	26(NE)	Present study
	6.0(SE)	28(SE)	
	3.0(W)	30(W)	
PMBI	1.0	32	Bora
	1.0	32	CRUST1.0
	1.0(NE)	33(NE)	Present study
	1.0(SE)	34 (SE)	
	1.0(W)	30(W)	

sampling model, and the number of inversion iterations.

Since only the crustal velocity structure is inversed, in order to avoid the noise data after the main seismic phases (such as Ps, PpPs, PpSs and PsPs) from interfering with the inversion results, the inversion time of receiver function waveform is 5 before the first arrival P-wave In order to avoid the non uniqueness of the receiver function, we select the average value of 1000 S-wave velocity structure models with the minimum mismatch function as the final inversion model.

Finally, the S-wave velocity structure of three directions (NE, SE and W) of each seismic station is obtained (Figs. 7–11). Fig. 12 shows the waveform fitting diagram of receiver function in three directions (NE, SE and W) before and after inversion. Generally speaking, the receiver function corresponding to the best model fits well with the average receiver function waveform of actual observation receiver function. Since the sedimentary layer and crystalline basement are given in the initial model and search space, the S-wave velocity structure information of shallow sedimentary layer and crystalline basement is also obtained, and the corresponding receiver function waveform is well fitted within 0–3 s.

3. Discussion

In this study, the crustal velocity structure under five broadband seismic stations in Sumatra subduction zone is inversed by Teleseismic Receiver function method, and the thickness of sedimentary layer and crust beneath the stations are given (Table 4).

The thickness of sediments obtained at GSI, LHMI and MNAI stations is more than 3 km, and the thickness of sedimentary layer at GSI and LHMI stations is more than 6 km.

The GSI station is located on the accretionary wedge of the forearc ridge of the Sumatra subduction zone, adjacent to the bat fault zone (BF) (Fig. 13). A large amount of sediments scraped from the oceanic crust were deposited here. Many strong earthquakes or earthquakes with m ≥ 6 occurred around the station, and most of them were thrust type earthquakes (Fig. 13). The difference of receiver function waveforms in different directions implies the complex crustal and sedimentary structure beneath the GSI station (Fig. 8).

The LHMI station located in North Sumatra Basin has also deposited

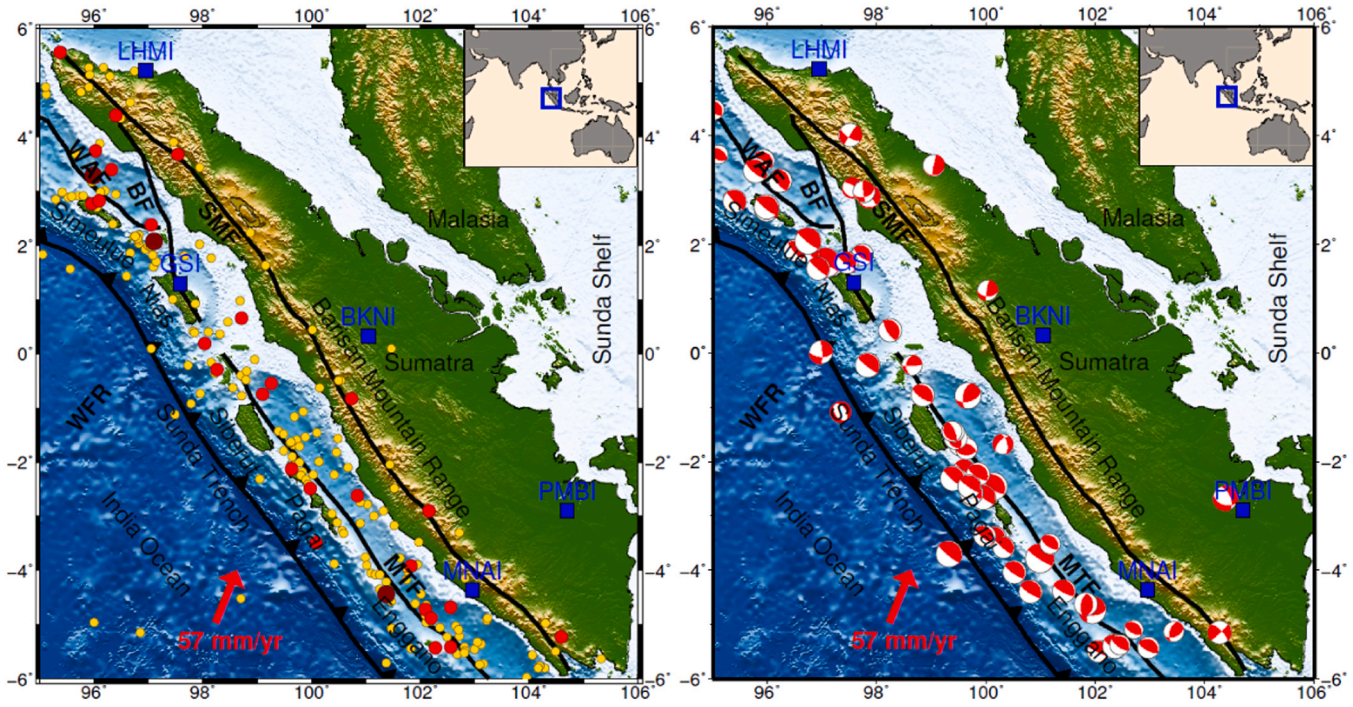

Fig. 13. Distributions of shallow-depth earthquakes (Focus depth ≦ 60 km) (Left) and focal mechanism solutions (Magnitude ≧ 6.0) (Right). Blue rectangles mark the five broadband stations. Yellow, red and dark red circles indicates the earthquakes for M 6.0–6.9, M∈7.0–7.9 and M ≧ 8.0. These data comes from USGS (January 1900–December 2017). The circles with red and white indicates the mechanism solutions. These data comes from the GCMT of Harvard University (1976–December 2013).

very thick sediments. Because the station is close to the Andaman Islands, the subduction angle of the Indo Australian plate to the Eurasian plate is small, and the resistance of the sediments above the oceanic crust is small in this area, which may be one of the reasons for the massive accumulation of the sediments. MNAI station is located on the near continental side of the egnano basin, which belongs to the edge of the forearc basin. Due to the scraping of the subducted oceanic crust, a large number of sediments were deposited here. BKNI and PMBI stations are located in the back arc basin of Sumatra subduction zone. Since there is no large amount of deposition of oceanic crust sediments, the thickness of sedimentary layer here is about 1 km (Table 4), mainly Quaternary sediments.

The crust types can be divided into oceanic crust (3–15 km), transitional crust (15–30 km) and continental crust (30–70 km). Oceanic type and continental type are the main types of crust. The crustal thickness of GSI and MNAI stations located in fore arc ridge and forearc basin is mainly between 25 and 30 km, belonging to transitional crust, while that of BKNI, LHMI and PMBI stations in back arc basin increases to 30–35 km, belonging to continental crust (Table 4). Sumatra fault zone is the largest fault in the study area, which passes through the whole Sumatra island. It is the boundary zone between the pre arc and back arc of Sumatra subduction zone system. According to the crustal structure of five stations (Table 4), it is also the boundary zone between oceanic crust and continental crust in this area.

According to the receiver function, the crustal thickness in the forearc basin increases from ~ 26 km (Table 4, GSI station) to 26–30 km (Table 4, MNAI station) on the near continental side of the forearc basin, while in the back arc basin, the crustal thickness increases to 30–36 km (Table 4, BNKI, LHMI and PMBI stations), and the subducted plate intersects the Moho plane at ~ 25 The depth is about 140 km from the deformation front. The transition from transitional crust to typical continental crust indicates that there are complex tectonic movements in this area.

A large number of shallow earthquakes occurred in the forearc area, suggesting strong deformation of the overlying plate in this area (Fig. 13). The focal depths of the representative large earthquakes in the fore arc area are about 80 km, except for the East mindavi earthquake in 2009, the focal depths of other major earthquakes (such as the great earthquake in North Sumatra Andaman region in 2004, the great earthquake near Nias island in 2005, the great earthquake in mingguru, South Sumatra in 2007, and the southern mindavi islands in South Sumatra in 2010) have the focal depths of about 80 km Between 20 and 35 km.

According to the dynamic Coulomb wedge model proposed by Wang and Hu, the forearc area of Sumatra subduction zone is located in the inner wedge of Coulomb wedge model, corresponding to the seismogenic zone of subduction zone interface. During the whole seismic cycle, the internal wedge usually maintains a stable state, providing a stable environment for the deformation of the forearc basin [38]. In the Mentawai fore arc area, the focal location reveals that there are two faults in the area, one is the Mentawai fault (MTF), which is located in the west of Mentawai basin (Fig. 13), and the other thrust fault is located in the east side of Mentawai basin [24]. Kumar pointed out that the dehydrated fluid from subducted plate migrated upward through the deep and large fault in the forearc area and did not form serpentinization in the downdip area in the forearc area of Sumatra subduction zone. Therefore, a wide seismogenic zone developed near the deep fault [23].

According to the induced mechanism of subduction zone earthquake, the formation mechanism of shallow earthquake is brittle fracture or friction slip [39]. For the strong shallow earthquake activity in Sumatra forearc area, the rupture area formed by the subduction of Indo-Australian Plate provides conditions for the stress release of large-scale mantle source earthquake activity in front of arc (such as brittle fracture and friction slip).

4. Conclusions

In this paper, the S-wave velocity structure under five fixed stations in Sumatra area is obtained by collecting and sorting the seismic data of seismic stations and combining with the geological and geophysical data of the study area, the following main conclusions and understandings are obtained:

(1) The thicknesses of the sedimentary layer obtained from the three azimuths of GSI, LHMI and MNAI stations are more than 3 km. The thicknesses of the sedimentary layer of GSI and LHMI stations are more than 6 km, which deposited a large number of marine sediments scraped from the oceanic crust. The differences of receiver function waveforms in different directions imply the complex structure of crust and sedimentary layer under GSI station. At BKNI and PMBI stations located in the back arc basin of Sumatra subduction zone, the thicknesses of sedimentary layer are about 1 km, mainly Quaternary sediments.
(2) The crustal thickness of the back arc basin is 30–36 km, while the crustal thickness in the forearc area increases from ~ 26 km of the forearc ridge to 26–30 km near the mainland side of the forearc basin, which implies that the dip limit (Plate-Moho contact belt) of the seismogenic zone in the forearc area is within 29–36 km, which also explains why shallow earthquakes (focal depth < 60 km) in the forearc area dominate.

CRediT authorship contribution statement

Xuelei Li: Writing – original draft, Writing – review & editing. **Yuan Wang:** Conceptualization. **Tianyao Hao:** Data curation. **Yuxin Yuan:** Investigation. **Zhuo Jia:** Software. **Jinpeng Luan:** Formal analysis, Methodology.

Declaration of Competing Interest

The authors declare the following financial interests/personal relationships which may be considered as potential competing interests: Xuelei Li reports financial support was provided by NSFC. Xuelei Li reports a relationship with National Natural Science Foundation of China that includes: funding grants. If there are other authors, they declare that they have no known competing financial interests or personal relationships that could have appeared to influence the work reported in this paper.

Acknowledgments

We would like to thank the editor and reviewers for their constructive comments. This research was supported by NSFC (42306084), Hunan Provincial Natural Science Foundation of China (2023JJ40223) and Scientific Research Fund of Hunan Provincial Education Department (21B0566).

References

[1] P. Molnar, P. Tapponnier, Cenozoic tectonics of Asia-effects of a continental collision, Science 189 (4201) (1975) 419–426.
[2] P. Patriat, J. Achache, India-Eurasia collision chronology has implications for crustal shortening and driving mechanism of plates, Nature 311 (1984) 615–621.
[3] S. Zang, Z. Wu, J. Ning, et al., The interaction of plates around china and its effect on the stress field in china, Part II: the influence of indian plate, Chin. J. Geophys. 35 (40) (1992) 428–440.
[4] S. Widiyantoro, R.D. van der Hilst, Structure and evolution of lithospheric slab beneath the Sunda Arc, Indonesia, Science 271 (5255) (1996) 1566–1570.
[5] C.J. Ammon, C. Ji, H.K. Thio, et al., Rupture process of the 2004 sumatra-andaman earthquake, Science 308 (5725) (2005) 1133.
[6] S. Zhu, H. Xing, F. Xie, et al., Simulation of earthquake processes by finite element method: the case of megathrust earthquakes on the Sumatra subduction zone, Chin. J. Geophys. 51 (2) (2008) 460–468.

[7] L. Dai, S. Li, C. Tao, et al., 3D numerical modeling of strain field in Sumatra area influenced by the coupling effect of subduction zone, Chin. J. Geophys. 53 (8) (2010) 1837–1851.
[8] W. Zhai, B. Zhang, L. Huang, et al., Comparisons of global coseismic displacements from several fault slip models for the 2004 Sumatra earthquake, Chin. J. Geophys. 59 (8) (2016) 2843–2858.
[9] S. Widiyantoro, R.D. van der Hilst, Mantle structure beneath Indonesia inferred from high-resolution tomographic imaging, Geophys. J. Int. 130 (1) (1997) 167–182.
[10] E. Hafkenscheid, S.J.H. Buiter, M.J.R. Wortel, et al., Modelling the seismic velocity structure beneath Indonesia: a comparison with tomography, Tectonophysics 333 (2001) 35–46.
[11] D.P. Zhao, Global tomographic images of mantle plumes and subducting slabs: insight into deep earth dynamics, Phys. Earth Planet. Inter. 146 (1) (2004) 3–34.
[12] J.S. Lei, D.P. Zhao, Global p-wave tomography: on the effect of various mantle and core phases, Phys. Earth Planet. Inter. 154 (1) (2006) 44–69.
[13] S. Richards, G. Lister, B.L.N. Kennett, A slab in depth: three-dimensional geometry and evolution of the Indo-Australian plate, Geochem. Geophys. Geosyst. 8 (12) (2007) 6051–6052.
[14] J.D. Pesicek, C.H. Thurber, S. Widiyantoro, et al., Complex slab subduction beneath northern Sumatra, Geophys. Res. Lett. 35 (20) (2008) 67–76.
[15] Z. Huang, D.P. Zhao, L. Wang, P wave tomography and anisotropy beneath Southeast Asia: insight into mantle dynamics, J. Geophys. Res. 120 (7) (2015) 5154–5174.
[16] R. McCaffrey, Slip vectors and stretching of the Sumatran Fore-Arc Basin, Geology 19 (9) (1991) 881–884.
[17] R. McCaffrey, Oblique plate convergence, slip vectors, and forearc deformation, J. Geophys. Res.-Solid Earth 97 (B6) (1992) 8095–8915.
[18] O. Bellier, M. Sebrier, Is the slip rate variation on the great Sumatran Fault accommodated by fore-arc stretching, Geophys. Res. Lett. 22 (15) (1995) 1969–1972.
[19] J.A. Malod, B.M. Kemal, The Sumatra Margin: oblique subduction and lateral displacement of the accretionary prism, Geol. Soc. Lond. Spec. Publ. 106 (1996) 19–28.
[20] M. Diament, H. Harjono, K. Karta, et al., Mentawai Fault zone off Sumatra–a new key to the geodynamics of western Indonesia, Geology 20 (3) (1992) 259–262.
[21] S.C. Singh, N.D. Hananto, A.P.S. Chauhan, et al., Evidence of active backthrusting at the NE Margin of Mentawai Islands, SW Sumatra, Geophys. J. Int. 180 (2) (2009) 703–714.
[22] D.E. Karig, S. Suparka, G.F. Moore, et al., Structure and Cenozoic evolution of the Sundra Arc in the central Sumatran Region, AAPG Mem. 29 (1978) 223–237.
[23] P. Kumar, H. Kawakatsu, Imaging the seismic lithosphere-asthenosphere boundary of the oceanic plate, Geochem. Geophys. Geosyst. 12 (1) (2013).
[24] R. Collings, D. Lange, A. Rietbrock, et al., Structure and seismogenic properties of the Mentawai segment of the Sumatra subduction zone revealed by local earthquake travel time tomography, J. Geophys. Res. 117 (B1) (2012) 280–290.
[25] C.A. Langston, Structure under Mount Rainier, Washington, Inferred from Teleseismic Body Waves, J. Geophys. Res. 84 (1979) 4749–4762.
[26] T.J. Owens, G. Zandt, S.R. Taylor, Seismic evidence for an ancient rift beneath the Cumberland Plateau, Tennessee – a detailed analysis of broad-band teleseismic P-waveforms, J. Geophys. Res. 89 (1984) 7783–7795.
[27] G. Kosarev, R. Kind, S.V. Sobolev, et al., Seismic evidence for a detached Indian lithospheric mantle beneath Tibet, Science 283 (1999) 1306–1309.
[28] T. Shibutani, M. Sambridge, B. Kennett, Genetic algorithm inversion for receiver functions with application to crust and uppermost mantle structure beneath eastern Australia, Geophys. Res. Lett. 23 (1996) 1829–1832.
[29] L.P. Vinnik, C. Reigber, I.M. Aleshin, et al., Receiver function tomography of the central Tien Shan, Earth Planet. Sci. Lett. 225 (2004) 131–146.
[30] X.H. Yuan, J. Ni, R. Kind, et al., Lithospheric and upper mantle structure of southern Tibet from a seismological passive source experiment, J. Geophys. Res. 102 (1997) 27491–27500.
[31] L.P. Zhu, H. Kanamori, Moho depth variation in southern California from teleseismic receiver functions, J. Geophys. Res. 105 (2000) 2969–2980.
[32] D.K. Bora, K. Borah, A. Goyal, Crustal shear-wave velocity structure beneath Sumatra from receiver function modeling, J. Asian Earth Sci. 121 (2016) 127–138.
[33] Z.W. Li, T.Y. Hao, Y. Xu, et al., A global optimizing approach for waveform inversion of receiver functions, Comput. Geosci. 36 (2010) 871–880.
[34] M.S. Sambridge, Non-linear arrival time inversion: Constraining velocity anomalies by seeking smooth models in 3-D, Geophys. J. Int. 102 (1990) 653–677.
[35] C.J. Ammon, G.E. Randall, G. Zandt, On the nonuniqueness of receiver function inversions, J. Geophys. Res. 95 (1990) 15303–15318.
[36] N. Harmon, T. Henstock, F. Tilmann, et al., Shear velocity structure across the Sumatran Forearc-Arc, Geophys. J. Int. 189 (3) (2012) 1306–1314.
[37] K.A. Macpherson, D. Hidayat, S.H. Goh, Receiver function structure beneath four seismic stations in the Sumatra region, J. Asian Earth Sci. 46 (46) (2012) 161–176.
[38] K. Wang, Y. Hu, Accretionary prisms in subduction earthquake cycles: the theory of dynamic Coulomb wedge, J. Geophys. Res. 111 (B6) (2006) B06410.
[39] C. Frohlich, Deep Earthquakes, Cambridge University Press, Cambridge, 2006, pp. 1–574.
[40] K. Kieling, R. Wang, S. Hainzl, Energy constrained rise time scaling for ground motion modelling in a layered earth model, Agu Fall Meeting, 2011.

Xue-lei Li received his PhD degree at University of Chinese Academy of Sciences (Institute of Geology and Geophysics, Chinese Academy of Sciences), China in 2018 and then worked as a postdoc at Innovation Academy for Precision Measurement Science and Technology, Chinese Academy of Sciences. He joined Hunan University of Technology and Business in 2020 and has worked as the associate dean since 2024. He has published more than 10 papers in the mainstream academic journals across geology, geophysics and geodesy.